Czochralski growth and characterization of the multicomponent garnet $(Lu_{1/4}Yb_{1/4}Y_{1/4}Gd_{1/4})_3Al_5O_{12}$

Matheus Pianassola,[1,2,*] Luis Stand,[1,3] Madeline Loveday,[1,2] Bryan C. Chakoumakos,[4] Merry Koschan,[1] Charles L. Melcher,[1,2,3] and Mariya Zhuravleva[1,2]

[1]*Scintillation Materials Research Center, University of Tennessee, Knoxville, Tennessee 37996, USA*
[2]*Department of Materials Science and Engineering, University of Tennessee, Knoxville, Tennessee 37996, USA*
[3]*Department of Nuclear Engineering, University of Tennessee Knoxville, Tennessee 37996, USA*
[4]*Neutron Scattering Division, Oak Ridge National Laboratory, Oak Ridge, Tennessee 37831, USA*

(Received 15 June 2021; accepted 4 August 2021; published 18 August 2021)

This work demonstrates the potential for practical scalable growth of complex garnets and evaluates the implications of a multicomponent composition in the optical quality and elemental distribution of a Czochralski-grown crystal. Our experimental approach was designed to elucidate the relation between a complex garnet composition $(Lu_{1/4}Yb_{1/4}Y_{1/4}Gd_{1/4})_3Al_5O_{12}$, crystal growth parameters, crystal structural, and elemental homogeneity. Our hypothesis is that combining multiple rare earths (REs) that will fractionally occupy the dodecahedral site in the aluminum garnet structure will result in a stable, single garnet compound that can be grown by the Czochralski method. Single-crystal and powder x-ray diffraction indicated a single garnet phase with an increasing unit cell volume from seed to tail. In addition, we propose that the pattern of elemental segregation will be based on the deviation of the ionic radius of each constituent RE from the average RE ionic radius of the multicomponent garnet. Electron probe microanalysis revealed that ions that are smaller than that average (Lu^{3+} and Yb^{3+}) are preferentially incorporated in the crystal, while elements that are larger than that average (Gd^{3+}) are rejected. The ionic radius of Y^{3+} is close to that average and yttrium segregation was minimal. The concentrations of the four REs are closer to stoichiometric on the tail end of the boule. Scanning electron microscopy and energy-dispersive x-ray spectroscopy analysis reveal Gd-rich inclusions with eutectic microstructures in the tail end of the boule.

DOI: 10.1103/PhysRevMaterials.5.083401

I. INTRODUCTION

The surprising phase stabilization [1] and functional properties [2] of high-entropy oxide ceramics have inspired the investigation into the crystal growth of complex oxides. Oxides containing five or more cations in equiatomic amounts can have an entropy-stabilized single phase [1]. This class of oxides meets the criteria for high configurational entropy ($\Delta S_{conf} \geqslant 1.5R$, where R is the gas constant [3]), but in some cases the stabilization of a single phase is not solely entropy related [4,5]. For this reason, the term "multicomponent oxide" is used to avoid implying an entropy-driven stabilization. In this current work, "multicomponent" indicates a composition with four or more types of cations that are expected to fractionally occupy the same crystallographic site. Interesting properties of multicomponent oxides include superionic conductivity [6], phosphorescence [7], and lasing [8]. In an effort to study complex compositions in single-crystal form, thin films have been produced [9–16]. More recently, multicomponent oxides have also been reported as bulk crystals, grown by the micro-pulling-down (mPD) [17], floating zone [18], and Czochralski (Cz) [19] methods.

To date, only a few reports focus on multicomponent oxides grown by a scalable bulk growth method such as Cz growth [19–21], which is commercially used to grow bulk semiconductor, scintillator, and laser crystals [22]. These reports describe the Cz growth of borates containing three or more cations in close to equiatomic amounts. Although the chemical composition of borate crystals was found to be relatively homogeneous along the growth direction, Cz crystals of other compositions may exhibit element segregation. As an example, the preferential incorporation of smaller cations has been demonstrated in multicomponent rare-earth aluminum garnets grown by the mPD method [17].

The mPD method is advantageous for growing crystals of excellent quality and homogeneous composition. This crystal growth method is based on directionally solidifying the melt as it is pulled down from a small crucible through a capillary channel, which separates the growth interface from the bulk of the melt. A thin (<1 mm thick) molten zone is located between the bottom of the crucible and the crystal. Rejected elements do not diffuse back into the crucible but segregate toward the periphery of the molten zone and are incorporated into the crystal. This results in radial composition gradients, while the axial elemental distribution is relatively homogeneous [23].

Significant differences in elemental distribution are expected between multicomponent garnets grown by the mPD and Cz methods, in that an axial composition gradient is expected for Cz-grown multicomponent crystals. Cz growth is based on directionally solidifying the melt by pulling the

*mpianass@vols.utk.edu

growing crystal upward out of the melt. There is no capillary channel, and the growing crystal is in contact with the bulk of the molten material. Rejected elements stay in the melt, leading to crystals with concentration gradients in the axial direction [24].

Additionally, the effects of melt flow on element incorporation are much more significant in Cz crystals due to the larger quantity of melt. In the Cz method, buoyancy-driven convection, Marangoni flow, and rotational (forced) convection affect the melt composition at the growth interface, impacting the radial element distribution [25–27]. In mPD growth, only the melt flows in the molten zone affect the composition at the growth interface; buoyancy-driven convection is negligible due to the small volume of melt, while Marangoni flow is dominant [23].

As the investigation of multicomponent aluminum garnets scales up from the mPD to the Cz technique, it is important to assess the implications of a disordered cation sublattice on the compositional homogeneity and optical quality of a Cz crystal. Rare-earth (RE) aluminum garnet crystals have the general formula $RE_3Al_5O_{12}$ and are commercially produced for lasing and scintillation applications [28,29]. Composition engineering has optimized functional properties by admixing up to three elements in the RE or Al sites [30–33]. Adding more elements into the composition may result in improved performance, but elemental segregation and poor optical quality in a Cz crystal may lead to an inconsistency in properties along the boule.

Most studies of composition homogeneity of Cz crystals focus on investigating the segregation of a dopant element, because functional properties rely on its uniform distribution in the crystal [34–42]. Investigation of distribution of the primary constituent cations in crystals with complex compositions, which is the focus of this work, is of equal importance. Studies of the distribution of primary cations are limited to compositions in which no more than three elements compete for the same crystallographic site [20,21,43–49]. Here we demonstrate the Cz crystal growth and assess the extent of an axial concentration gradient, optical quality, and crystal structure of the four-component equiatomic aluminum garnet $(Lu_{1/4}Yb_{1/4}Y_{1/4}Gd_{1/4})_3Al_5O_{12}$. This compound is a medium entropy material with a $\Delta S_{conf} = 1.4R$ [3].

The composition contains four primary constituent RE elements that were selected from a relatively wide ionic radii range of 0.977 – 1.053 Å to investigate the dependence of element incorporation on cation size [50]. For simplicity, yttrium is referred to here as a RE element. Two REs lie at the shorter end of the range, Lu^{3+} (0.977 Å) and Yb^{3+} (0.985 Å), while Y^{3+} (1.019 Å) lies around the middle, and Gd^{3+} (1.053 Å) at the larger end of the range [50]. Small REs are expected to be more readily incorporated in garnet crystals since larger REs disrupt the Al-O framework [17,51]. As larger REs are rejected by the growing crystal, they become enriched in the melt. Since the incorporation of ions in the crystal is proportional to their concentration in the melt, from the top to the bottom of the crystal the concentration of smaller REs is expected to decrease, while the concentration of larger REs is expected to increase. Consequently, the unit cell volume will expand, from the seed end to the tail end. This lattice misfit along the boule may cause lattice strain, which can result in defect formation due to internal stresses.

TABLE I. $(Lu_{1/4}Yb_{1/4}Y_{1/4}Gd_{1/4})_3Al_5O_{12}$ Czochralski crystal portions and respective dimensions.

Crystal portion	Dimension
Neck	20 mm length, 7 mm diameter
Shoulder	65 mm length, 44 °
Cylinder	55 mm length, 30 mm diameter
Tail	55 mm length, 2 mm diameter

II. EXPERIMENTAL SECTION

A. Materials and crystal growth

A $(Lu_{1/4}Yb_{1/4}Y_{1/4}Gd_{1/4})_3Al_5O_{12}$ crystal was grown by the Czochralski method using a Cyberstar Oxypuller 05-03 growth station. Powders of Lu_2O_3, Yb_2O_3, Y_2O_3, Gd_2O_3, and Al_2O_3 of at least 99.99% purity were mixed in stoichiometric quantities and the mixture was placed into an iridium crucible that is 60 mm in both height and diameter. The powder mixture was melted by inductively heating the crucible in a flowing nitrogen atmosphere with approximately 0.2 vol % of oxygen. Crystal growth was initiated on a $Lu_3Al_5O_{12}$: Ce seed oriented in the ⟨111⟩ direction. The rotation and pulling rates were 11 rpm and 1 mm/h, respectively. Table I contains the crystal dimensions. A total of 525 g of material was pulled from the melt, which corresponds to 67% of the initial charge. After the active growth phase was finished, the crystal was gradually cooled over 48 h.

Five cross-sectional samples of the crystal were cut for characterization; each sample was 5 mm thick. Sample S was cut 5 mm below the seed in the neck region. Samples C1–C3 were cut from the cylindrical region and their respective original locations were 1 mm away from the shoulder, approximately the middle of the cylinder, and 1 mm away from the tail. Sample T was cut 5 mm away from the tip of the tail. A schematic representation of the crystal portions and the five cross-sectional samples is shown in Fig. 1.

B. Optical microscopy

Half-diameter slices from samples C1–C3 were polished and inclusions were imaged with Keyence VHX-1000 and Zeiss Axio Observer A1 optical microscopes.

C. Optical transmission

Plates of 0.5 mm thickness cut from samples C1–C3 were polished for optical transmission measurements. A Varian Cary 5000 UV-VIS-IR spectrophotometer was used to acquire optical transmission spectra in the range of 200–800 nm.

D. Powder x-ray diffraction

A half-diameter slice from each of the five samples was ground in a mortar for phase analysis via powder x-ray diffraction (XRD). A Panalytical Empyrean diffractometer was used in the Bragg-Brentano geometry using a Cu $K\alpha$ x-ray source ($\lambda_{K\alpha1} = 1.5405$ Å, $\lambda_{K\alpha2} = 1.5443$ Å) at 45 kV and 40 mA.

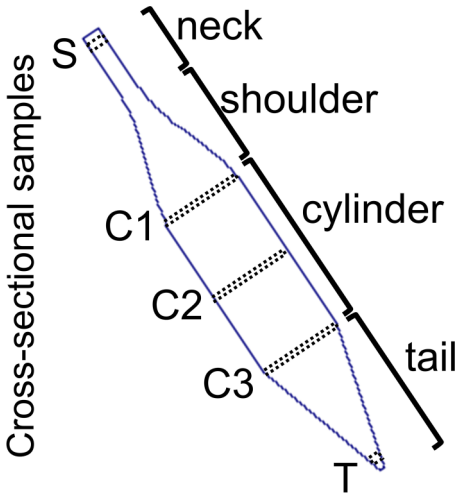

FIG. 1. Schematic representation of the $(Lu_{1/4}Yb_{1/4}Y_{1/4}Gd_{1/4})_3Al_5O_{12}$ crystal (blue). Crystal portions are named on the right side of the figure. Dotted lines indicate the regions from which the five cross-sectional samples were cut for characterization; sample IDs are shown on the left side of the image.

Phase analysis and lattice parameter evaluation were done via Rietveld refinement using the General Structure Analysis System II software (GSASII).

E. Single-crystal x-ray diffraction

For further assessment of the crystal structure, single-crystal XRD data were obtained for samples C1–C3. A crystal portion was cut from the center of each sample. Sample dimensions are given in Table S-I in the Supplemental Material [52]. Each of the three portions was suspended in Paratone oil on a plastic loop attached to a copper goniometer. A Rigaku XtaLAB PRO diffractometer with graphite monochromated Mo $K\alpha$ radiation (50 kV, 40 mA, $\lambda = 0.710\,73$ Å) equipped with a Rigaku HyPix-6000HE detector and an Oxford N-HeliX cryocooler was used to collect single-crystal diffraction data at 250 K.

The Rigaku Oxford Diffraction CRYSALISPRO software was used for peak indexing and integration [53]. The SCALE3 ABSPACK algorithm as implemented in CRYSALISPRO was used to apply an empirical absorption correction. Data processing and structure refinement were performed using the SHELXL-2013 and WINGX software packages [54,55]. The structure refinements were made with the scale factor, an extinction parameter, anisotropic atomic displacement parameters, and oxygen atom positional coordinates.

F. Electron probe microanalysis

To evaluate the elemental distribution in the crystal, samples C1–C3 were subjected to electron probe microanalysis (EPMA). A 2 mm thick full-diameter slice was cut from each sample and embedded in epoxy. A CAMECA SX100 Electron Microprobe equipped with high-speed backscattered electron (BSE) detectors and four wavelength-dispersive spectrometers (WDSs) was used at 15 kV and 30 nA. Images were acquired by detecting the backscattered electrons and

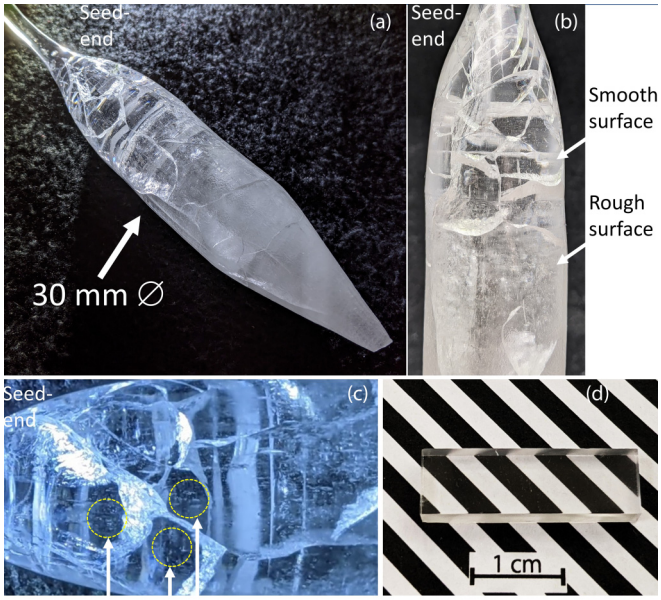

FIG. 2. (a) As-grown $(Lu_{1/4}Yb_{1/4}Y_{1/4}Gd_{1/4})_3Al_5O_{12}$ boule; crystal is transparent and heavily cracked. (b) In the cylindrical region, there is a clear transition from smooth to rough surface. (c) Macroscopic inclusions in the shoulder region; similar inclusions were observed throughout the whole crystal. (d) Polished pixel of $23 \times 5 \times 5$ mm cut from sample C1.

compositional data were obtained from the characteristic x rays by WDS. The probe point size was 1 μm and the diameter of the excitation area was in the 2–3 μm range. Data were collected in 1 mm steps to generate radial distribution profiles.

G. Scanning electron microscopy and energy-dispersive spectroscopy

To investigate the morphology and elemental composition of inclusions, a small crystal fragment was cut from sample C3, which has a higher concentration of inclusions compared to samples C1 and C2. The fragment was polished to expose the inclusions to the surface. A Zeiss EVO MA15 scanning electron microscope (SEM) equipped with a Bruker xFlash 6130 energy-dispersive x-ray spectrometer (EDS) was used to image the inclusions and analyze their elemental composition.

III. RESULTS AND DISCUSSION

A. Grown crystal and macroscopic defects

A transparent $(Lu_{1/4}Yb_{1/4}Y_{1/4}Gd_{1/4})_3Al_5O_{12}$ crystal was grown, demonstrating the potential for practical Cz growth of complex multicomponent aluminum garnets. The melt behavior was typical for single RE aluminum garnets, with visible convective melt flow, indicating good mixing. As shown in Fig. 2(a), the crystal has a well-controlled shape. The crystal surface is smooth on the seed end and rough on the tail end, as seen in Fig. 2(b). The rough surface is due to thermal etching. The crystal was cooled inside the iridium crucible, which explains a more pronounced thermal etching on the tail end.

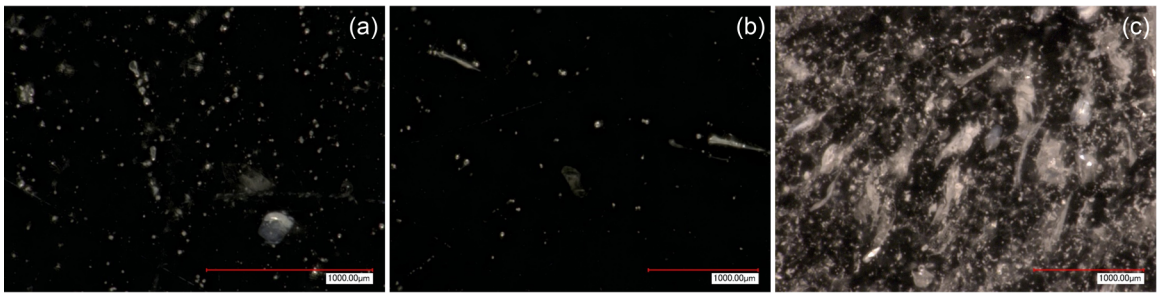

FIG. 3. Optical microscope images of internal defects in samples (a) C1, (b) C2, and (c) C3. Sample C3 has cloudlike defects in addition to a higher concentration of inclusions compared to C1 and C2. Images obtained with a Keyence VHX-1000 microscope.

Although the crystal is cracked and contains internal macroscopic defects, defect-free samples were obtained from the cylindrical region. Only a few cracks reach the center of the crystal, and they may originate from the lattice strain that results from the difference in ionic radii between the REs in the composition. Macroscopic inclusions can be observed by the naked eye, as seen in the shoulder section in Fig. 2(c). Similar internal defects were observed throughout the whole crystal. Nevertheless, even at this early stage of development, samples with high optical quality could be obtained from the cylindrical portion of the boule; Fig. 2(d) shows a pixel cut from sample C1.

Samples C1–C3 contain inclusions and C3 also has cloudlike defects. Optical microscopy images of samples C1–C3 are presented in Figs. 3(a)–3(c), respectively. Samples C1 and C2 have lower concentrations of inclusions than C3. Also, cloudlike defects were observed in C3. Cloudlike defects may result from microcracks that formed due to a more pronounced lattice strain on the tail end of the crystal, which will be discussed in Sec. III B. An image of an inclusion in C3 is shown with higher magnification in Fig. 4. A higher concentration of inclusions on the tail end is typical of defect-containing Cz-grown crystals [56–58]. This is due to a higher concentration of segregated species at the growth interface and a reduced convective melt flow due to a reduced depth of the melt.

Cloudlike defects and a higher concentration of inclusions are responsible for a diminished optical transmission on the tail end compared to the seed end. In Fig. 5 the optical transmission spectra of samples C1–C3 are compared. In the 350–800 nm wavelength range, the optical transmittance of samples C1 and C2 are in the range of 68%–76% and 63%–65%, respectively. This transmittance range decreases to 38%–42% for sample C3 due to the higher concentration of defects and inclusions. Gd^{3+} electronic transitions were observed at ∼275 and ∼310 nm and are indicated in Fig. 5.

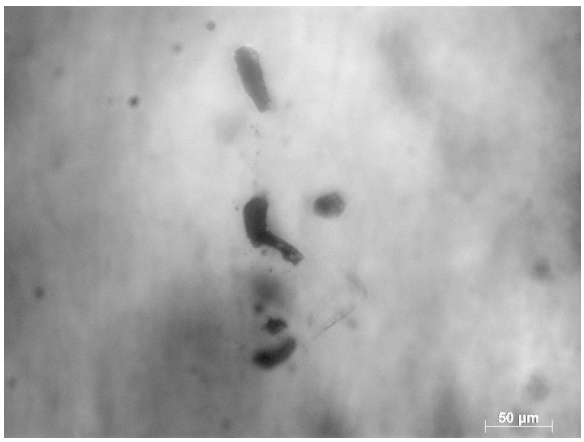

FIG. 4. Optical image of inclusions in sample C3. Image obtained with a Zeiss Axio Observer A1 microscope.

B. Crystal structure

Powder and single-crystal XRD measurements reveal that the $(Lu_{1/4}Yb_{1/4}Y_{1/4}Gd_{1/4})_3Al_5O_{12}$ crystal is a single garnet phase with an $Ia\bar{3}d$ space group. In Fig. 6(a), the powder XRD patterns of samples S, C1–C3, and T are compared to a reference pattern for $Er_3Al_5O_{12}$ (ICSD 62615); the reflection peaks for the samples match well with the reference. The peak splitting is due to the overlap of Cu $K\alpha_1$ and Cu $K\alpha_2$ reflections. Among all RE elements, the ionic radius of Er^{3+} (1.004 Å) is the closest one to the average theoretical ionic radius of the REs in $(Lu_{1/4}Yb_{1/4}Y_{1/4}Gd_{1/4})_3Al_5O_{12}$, which is (1.009 Å) [50]. Rietveld refinement of the powder XRD patterns reveals a single garnet phase and an increasing lattice parameter from seed to tail as shown in Fig. 6(b). Refinement

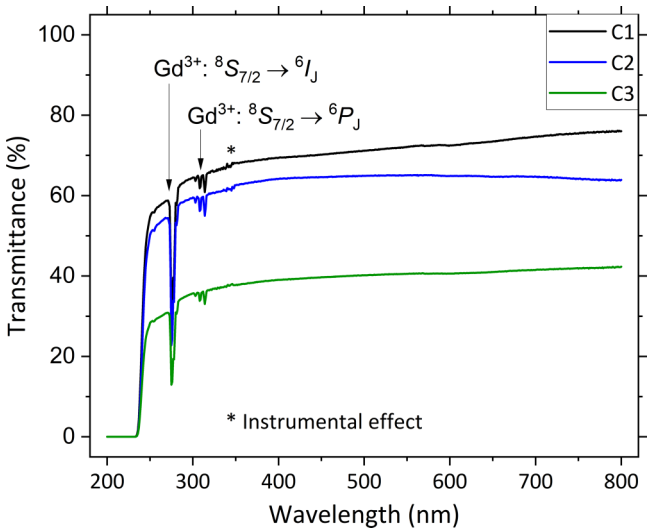

FIG. 5. Optical transmission spectra. The transmittance decreases from seed to tail end due to an increasing concentration of defects and inclusions.

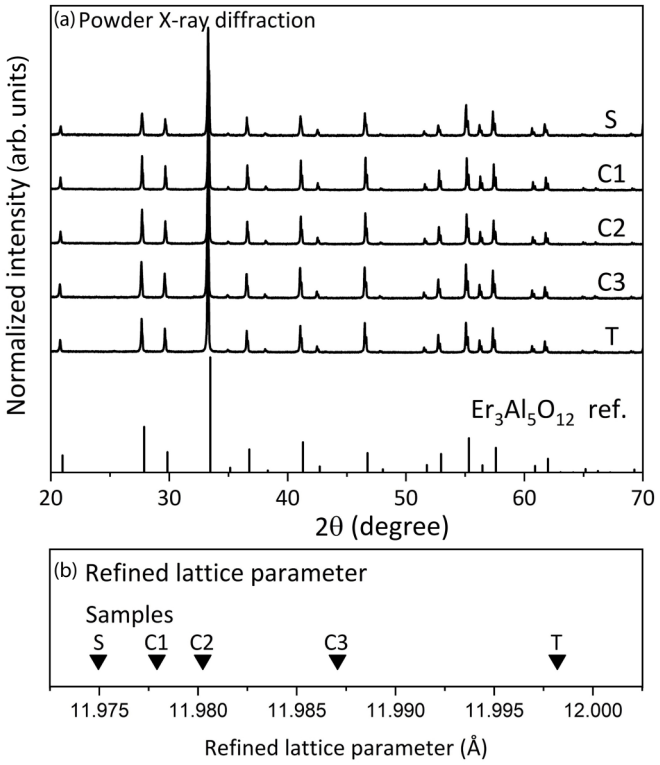

FIG. 6. (a) Powder XRD patterns of samples S, C1–C4, and T indicate a single garnet phase. A reference pattern of $Er_3Al_5O_{12}$ (ICSD 62615) is plotted for comparison. (b) Lattice parameter obtained via Rietveld refinement of powder XRD data for the five samples. Lattice parameter increases from seed to tail.

data for the single-crystal XRD patterns of samples C1–C3 also indicate a single garnet phase and an increasing lattice parameter from seed to tail. Single-crystal XRD refinement parameters are in Table S-I and the fractional atomic coordinates and equivalent isotropic displacement parameters are in Table S-II in the Supplemental Material [52]. No obvious diffuse scattering was observed in the x-ray patterns, which indicates no short-range clustering of REs.

The increasing lattice parameter from seed to tail indicates a gradient in crystal composition in the growth direction. This is due to the accumulation of larger REs in the melt as growth progressed. The incorporation of elements in the crystal is proportional to their concentration in the melt. Therefore, a higher concentration of the larger REs in the melt, which were rejected earlier in the growth process, led to a higher concentration of them toward the tail of the crystal. This can be confirmed by the fact that the difference in lattice parameter between consecutive samples is not monotonic, and becomes greater toward the tail of the crystal, as shown in Fig. 6(b).

The higher concentration of larger elements on the tail end also results in a more pronounced lattice strain since large elements are geometrically disadvantaged in the RE aluminum garnet structure. Rietveld refinement of powder XRD data revealed an increase in the isotropic microstrain parameter from seed to tail end. The unitless microstrain peak broadening fraction of samples S, C1, C2, C3, and T are 562, 1038, 1044, 1055, and 1250, respectively. This explains the more intense cracking on the tail end.

C. Elemental distribution

An axial composition gradient in $(Lu_{1/4}Yb_{1/4}Y_{1/4}Gd_{1/4})_3Al_5O_{12}$ indicates a rejection of larger REs by the growing crystal. In Fig. 7, EPMA radial elemental profiles are shown for samples C1–C3. The nominal stoichiometric concentration of each RE element is 3.75 at. % and the crystal composition is closer to stoichiometric in C3, which results in a more pronounced lattice strain on the tail end due to differences in RE^{3+} ionic radius. This results in the formation of microcracks which appear as the cloudlike defects discussed in Sec. III A. A general trend in the elemental profiles of smaller Lu^{3+} and Yb^{3+} ions is observed across the three samples: both ions have similar, higher than nominal concentrations that decrease consistently from ∼4.5 at. % in C1 to ∼4.0 at. % in C3. All three samples have Y^{3+} ions in close to stoichiometric amounts; a consistent, slight increase in Y^{3+} concentration is observed from C1 through C3. All samples are depleted in larger Gd^{3+} ions; the concentration of Gd^{3+} increases consistently from ∼2.25 at. % in C1 to

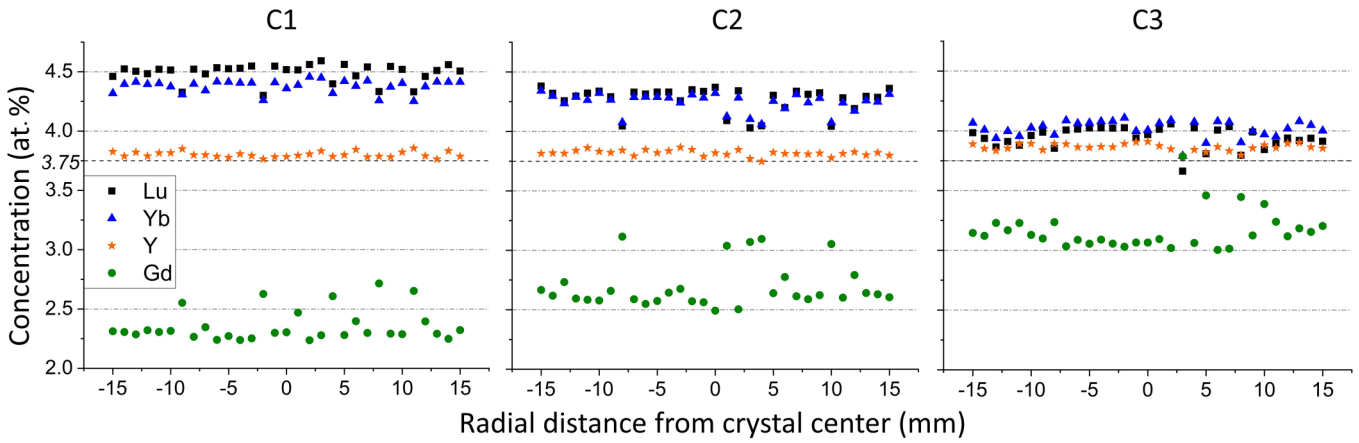

FIG. 7. EPMA radial concentration profiles of samples C1 (left), C2 (center), and C3 (right). The legend on the left applies to all graphs. On the horizontal axis, zero represents the center of the crystal, while −15 or +15 mm represents the last measurement toward the outer surface of the cylindrical crystal. On the vertical axis, 3.75 at. % indicates the nominal concentration of RE ions.

TABLE II. EDS elemental composition results for areas 1–6 shown in the SEM image in Fig. 8. In the approximate stoichiometry of each area, the stoichiometric coefficient of "RE" represents the combined concentration of each RE.

		EDS elemental composition (at. %), error <0.001 at. %						
Area	Point from Fig. 8	Lu	Yb	Y	Gd	Al	O	Stoichiometry
	Nominal composition	3.75	3.75	3.75	3.75	25.00	60.00	$RE_3Al_5O_{12}$
Outside the inclusion	1	4.28	4.11	4.44	3.43	28.67	55.07	$RE_{3.3}Al_{5.7}O_{11.0}$
	2	3.85	3.81	4.40	3.22	27.90	56.82	$RE_{3.1}Al_{5.6}O_{11.4}$
Lighter area in the inclusion	3	2.01	2.02	3.01	6.75	34.05	52.16	$RE_{2.8}Al_{6.8}O_{10.4}$
	4	1.96	2.06	2.96	6.88	31.60	54.54	$RE_{2.8}Al_{6.3}O_{10.9}$
Darker area in the inclusion	5	0.70	0.67	0.63	0.79	41.68	55.53	$RE_{0.6}Al_{8.3}O_{11.1}$
	6	0.68	0.67	0.64	1.00	38.67	58.34	$RE_{0.6}Al_{7.7}O_{11.7}$

~3.1 at. % in C3. Based on the EPMA results, we conclude that larger ions are rejected by the growing crystal, as expected. This is consistent with the observed expansion in unit cell volume from seed to tail.

The rejection of Gd^{3+} primary constituent ions in $(Lu_{1/4}Yb_{1/4}Y_{1/4}Gd_{1/4})_3Al_5O_{12}$ is consistent with the rejection of dopants (typically used in small concentrations) that are larger than the substituted ion in garnet crystals [34–42]. Larger dopants have a segregation coefficient $k < 1$ and their concentration in the melt increases during the growth. As a result, the concentration of larger dopants increases in the crystal from seed to tail. Based on the EPMA results shown in Fig. 7, we can infer that in $(Lu_{1/4}Yb_{1/4}Y_{1/4}Gd_{1/4})_3Al_5O_{12}$ the segregation coefficient is $k > 1$ for both Lu^{3+} and Yb^{3+}, $k \approx 1$ for Y^{3+}, and $k < 1$ for Gd^{3+}.

As seen in Fig. 7, in all samples the radial concentration profiles of Y^{3+} ions are relatively constant, while sharp variations are observed in the profiles of Lu^{3+}, Yb^{3+}, and Gd^{3+}. Local valleys in the concentration profiles of both Lu^{3+} and Yb^{3+} are observed; in general, the magnitude of these valleys is similar for both REs. These decreases in the concentration of Lu^{3+} and Yb^{3+} are correlated with a pronounced, sharp increase in the concentration of the larger Gd^{3+}. These sharp features may result from composition variations in the melt at the growth interface due to the accumulation of Gd ions. Therefore, when the melt at the solid/liquid interface is locally rich in Gd^{3+}, a relatively higher amount of Gd^{3+} is incorporated. This would explain the peaks in the concentration profiles of Gd^{3+} and the associated valleys for Lu^{3+} and Yb^{3+}.

The composition homogeneity of multicomponent Cz crystals may depend on the type of compositional system. While the multicomponent aluminum garnet $(Lu_{1/4}Yb_{1/4}Y_{1/4}Gd_{1/4})_3Al_5O_{12}$ has an axial composition gradient, multicomponent RE borate crystals have a homogeneous composition [20,21], without any significant element segregation. Therefore, the axial composition gradient in multicomponent garnets may be characteristic of garnet crystals due to the rejection of larger elements by the crystal lattice.

D. Inclusions: Microstructure and elemental composition

Inclusions such as the ones seen in Fig. 4 have a eutectic microstructure and are rich in Gd. As seen in the SEM image of C3 in Fig. 8, the inclusions have a typical eutectic microstructure composed of lighter and darker phases that are continuously entangled in a three-dimensional interpenetrating network [59]. Table II has the EDS data that were collected from the six points indicated in Fig. 8 to assess the elemental composition outside and inside the inclusion. Outside the inclusion (points 1 and 2) the sample has similar amounts of Lu, Yb, Y, and is depleted in Gd. This is consistent with the EPMA results for sample C3 shown in Fig. 7. On the other hand, lighter areas in the inclusion (points 3 and 4) are significantly richer in Gd. Therefore, the sharp features in the Gd^{3+} concentration profile in Fig. 7 may correspond to areas with these eutectic inclusions. Darker areas in the inclusion (points 5 and 6) have lower, close to equiatomic amounts of REs and are richer in Al, indicating a secondary alumina phase that could not be detected via powder or single-crystal XRD.

One possible explanation for the formation of eutectic inclusions would be clustering of Gd^{3+} at the growth interface, which could result in localized variations in melt composition. In the phase diagrams of one-RE RE_2O_3-Al_2O_3 systems, a trend can be observed in the position of the eutectic formed between the one-RE garnet $RE_3Al_5O_{12}$ and Al_2O_3 [60,61]. The eutectic point is closer to the garnet stoichiometry as the ionic radius increases in the series of Lu, Yb, Y, and Gd; the position of the Al_2O_3 and $Gd_3Al_5O_{12}$ eutectic is the closest to the position of the garnet stoichiometry. In the case of multicomponent melts that are enriched in larger elements

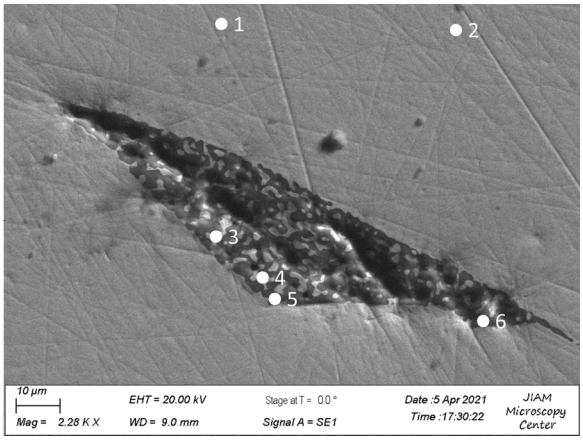

FIG. 8. SEM image of an inclusion with a eutectic microstructure in sample C3. Similar inclusions were observed in other areas of the sample. Table II has the EDS data collected for points 1–6 indicated in the image.

such as Gd, the probability of forming eutectic inclusions is increased.

To minimize the formation of defects in Cz-grown multicomponent garnets, growth parameters and composition could be optimized. A faster rotation rate is expected to intensify the forced melt convection and improve melt mixing and, therefore, elemental homogeneity in the growth interface. This effect would be more significant toward the end of the growth when the depth of the melt in the crucible is reduced, and buoyancy-driven convection is less pronounced [62]. Decreasing the relative amount of larger REs with respect to smaller REs in the nominal composition could minimize the formation of eutectic inclusions. In this case, the amount of REs would not be equiatomic. Additionally, off-stoichiometric melts have been shown to eliminate the formation of inclusions in garnet crystals [63]. In this case, the ratio of RE/Al could be slightly increased above the 3/5 stoichiometry.

IV. CONCLUSION

A multicomponent garnet crystal $(Lu_{1/4}Yb_{1/4}Y_{1/4}Gd_{1/4})_3Al_5O_{12}$ was successfully grown by the Cz method with a well-controlled shape. The Cz-grown $(Lu_{1/4}Yb_{1/4}Y_{1/4}Gd_{1/4})_3Al_5O_{12}$ crystal is cracked and contains eutectic inclusions and cloudlike defects. The crystal is a single garnet phase with increasing lattice parameters from seed to tail. Smaller REs have segregation coefficients $k > 1$ and are concentrated on the seed end, while larger REs have $k < 1$ and are concentrated in the tail end. Due to the variations in k among the REs, multicomponent garnets have an axial composition gradient of the primary constituent (or matrix) REs. This is analogous to the axial gradient in the dopant concentration seen in doped Cz-grown garnets.

We demonstrated the practical aspect of the scalable growth of complex garnet crystals, which had been previously reported only as miniature bulk crystals grown by the micro-pulling-down method. This opens a possibility of compositional engineering and growth of multicomponent garnets containing REs beyond the ones investigated here. Future work will focus on studying different combinations of REs to investigate the correlation between ionic radii, segregation behavior, and incorporation of inclusions. Varying the range of RE ionic radii and deviating from equiatomic ratios may allow tuning of crystal structure and functional properties.

ACKNOWLEDGMENTS

This project was supported by the NSF (Grant No. DMR 1846935). One of the authors is grateful for the support from the Center for Materials Processing, University of Tennessee. Electron microprobe measurements were performed at the Electron Microprobe Laboratory in the Department of Earth and Planetary Sciences at the University of Tennessee, Knoxville, with the assistance of M. McCanta and A. Patchen. X-ray diffraction experiments were performed at the Joint Institute for Advanced Materials Diffraction Facility located at the University of Tennessee, Knoxville. A portion of this research used resources at the Spallation Neutron Source, a Department of Energy Office of Science User Facility operated by the Oak Ridge National Laboratory.

[1] C. M. Rost, E. Sachet, T. Borman, A. Moballegh, E. C. Dickey, D. Hou, J. L. Jones, S. Curtarolo, and J. P. Maria, Entropy-stabilized oxides, Nat. Commun. **6**, 1 (2015).

[2] B. L. Musicó, D. Gilbert, T. Z. Ward, K. Page, E. George, J. Yan, D. Mandrus, and V. Keppens, The emergent field of high entropy oxides: Design, prospects, challenges, and opportunities for tailoring material properties, APL Mater. **8**, 040912 (2020).

[3] B. S. Murty, J. W. Yeh, and S. Ranganathan, *High-Entropy Alloys* (Elsevier, Butterworth-Heinemann, Oxford, 2014).

[4] R. Djenadic, A. Sarkar, O. Clemens, C. Loho, M. Botros, V. S. K. Chakravadhanula, C. Kübel, S. S. Bhattacharya, A. S. Gandhi, and H. Hahn, Multicomponent equiatomic rare earth oxides, Mater. Res. Lett. **5**, 102 (2017).

[5] M. Pianassola, M. Loveday, J. W. McMurray, M. Koschan, C. L. Melcher, and M. Zhuravleva, Solid-state synthesis of multicomponent equiatomic rare-earth oxides, J. Am. Ceram. Soc. **103**, 2908 (2020).

[6] D. Bérardan, S. Franger, D. Dragoe, A. K. Meena, and N. Dragoe, Colossal dielectric constant in high entropy oxides, Phys. Status Solidi RRL **10**, 328 (2016).

[7] G. Zhang, I. Milisavljevic, K. Grzeszkiewicz, P. Stachowiak, D. Hreniak, and Y. Wu, New optical ceramics: High-entropy sesquioxide X_2O_3 multi-wavelength emission phosphor transparent ceramics, J. Eur. Ceram. Soc. **41**, 3621 (2021).

[8] X. Chen and Y. Wu, High-entropy transparent fluoride laser ceramics, J. Am. Ceram. Soc. **103**, 750 (2020).

[9] V. Jacobson, D. Diercks, B. To, A. Zakutayev, and G. Brennecka, Thin film growth effects on electrical conductivity in entropy stabilized oxides, J. Eur. Ceram. Soc. **41**, 2617 (2021).

[10] T. X. Nguyen, Y. H. Su, J. Hattrick-Simpers, H. Joress, T. Nagata, K. S. Chang, S. Sarker, A. Mehta, and J. M. Ting, Exploring the first high-entropy thin film libraries: Composition spread-controlled crystalline structure, ACS Comb. Sci. **22**, 858 (2020).

[11] S. Sivakumar, E. Zwier, P. B. Meisenheimer, and J. T. Heron, Bulk and thin film synthesis of compositionally variant entropy-stabilized oxides, J. Visualized Exp. **2018**, e57746 (2018).

[12] Y. Sharma, B. L. Musico, X. Gao, C. Hua, A. F. May, A. Herklotz, A. Rastogi, D. Mandrus, J. Yan, H. N. Lee, M. F. Chisholm, V. Keppens, and T. Z. Ward, Single-crystal high entropy perovskite oxide epitaxial films, Phys. Rev. Materials **2**, 060404(R) (2018).

[13] Y. Sharma, A. R. Mazza, B. L. Musico, E. Skoropata, R. Nepal, R. Jin, A. V. Ievlev, L. Collins, Z. Gai, A. Chen, M. Brahlek, V. Keppens, and T. Z. Ward, Magnetic texture in insulating single crystal high entropy oxide spinel films, ACS Appl. Mater. Interfaces **13**, 17971 (2021).

[14] J. L. Braun, C. M. Rost, M. Lim, A. Giri, D. H. Olson, G. N. Kotsonis, G. Stan, D. W. Brenner, J.-P. Maria, and P. E. Hopkins, Charge-induced disorder controls the thermal conductivity of entropy-stabilized oxides, Adv. Mater. **30**, 1805004 (2018).

[15] P. B. Meisenheimer, T. J. Kratofil, and J. T. Heron, Giant enhancement of exchange coupling in entropy-stabilized oxide heterostructures, Sci. Rep. **7**, 1 (2017).

[16] R. K. Patel, S. K. Ojha, S. Kumar, A. Saha, P. Mandal, J. W. Freeland, and S. Middey, Epitaxial stabilization of ultra thin films of high entropy perovskite, Appl. Phys. Lett. **116**, 071601 (2020).

[17] M. Pianassola, M. Loveday, B. C. Chakoumakos, M. Koschan, C. L. Melcher, and M. Zhuravleva, Crystal growth and elemental homogeneity of the multicomponent rare-earth garnet $(Lu_{1/6}Y_{1/6}Ho_{1/6}Dy_{1/6}Tb_{1/6}Gd_{1/6})_3Al_5O_{12}$, Cryst. Growth Des. **20**, 6769 (2020).

[18] C. Kinsler-Fedon, Q. Zheng, Q. Huang, E. S. Choi, J. Yan, H. Zhou, D. Mandrus, and V. Keppens, Synthesis, characterization, and single-crystal growth of a high-entropy rare-earth pyrochlore oxide, Phys. Rev. Materials **4**, 104411 (2020).

[19] F. Liu, L. Dong, S. Cao, J. Chen, H. Xu, W. Han, and J. Liu, Crystal growth, structural characterization and laser operation of an $Yb_{0.19}Y_{0.34}Lu_{0.12}Gd_{0.35}Ca_4O(BO_3)_3$ mixed crystal, J. Cryst. Growth **558**, 126023 (2021).

[20] L. Gheorghe, F. Khaled, A. Achim, F. Voicu, P. Loiseau, and G. Aka, Czochralski growth and characterization of incongruent melting $La_xGd_ySc_z(BO_3)_4$ $(x+y+z=4)$ nonlinear optical crystal, Cryst. Growth Des. **16**, 3473 (2016).

[21] M. Greculeasa, A. Broasca, F. Voicu, S. Hau, G. Croitoru, G. Stanciu, C. Gheorghe, N. Pavel, and L. Gheorghe, Bifunctional $La_xNd_yGd_zSc_{4-x-y-z}(BO_3)_4$ crystal: Czochralski growth, linear and nonlinear optical properties, and near-infrared laser emission performances, Opt. Laser Technol. **131**, 106433 (2020).

[22] C. D. Brandle, Czochralski growth of oxides, J. Cryst. Growth **264**, 593 (2004).

[23] T. Fukuda and V. I. Chani, *Shaped Crystals: Growth by the Micro-Pulling-Down Technique* (Springer, Berlin, Heidelberg, 2007).

[24] C. D. Brandle, A. J. Valentino, and G. W. Berkstresser, Czochralski growth of rare-earth orthosilicates (Ln_2SiO_5), J. Cryst. Growth **79**, 308 (1986).

[25] J. R. Carruthers, Radial solute segregation in Czochralski growth, J. Electrochem. Soc. **114**, 959 (1967).

[26] A. D. W. Jones, Hydrodynamics of Czochralski growth—a review of the effects of rotation and buoyancy force, Prog. Cryst. Growth Charact. **9**, 139 (1984).

[27] S. Abbasoglu and I. Sezai, Three-dimensional modelling of melt flow and segregation during Czochralski growth of Ge_xSi_{1-x} single crystals, Int. J. Therm. Sci. **46**, 561 (2007).

[28] M. Nikl, A. Yoshikawa, K. Kamada, K. Nejezchleb, C. R. Stanek, J. A. Mares, and K. Blazek, Development of LuAG-based scintillator crystals—a review, Prog. Cryst. Growth Charact. Mater. **59**, 47 (2013).

[29] A. Ikesue, Y. L. Aung, T. Taira, T. Kamimura, K. Yoshida, and G. L. Messing, Progress in ceramic lasers, Annu. Rev. Mater. Res. **36**, 397 (2006).

[30] K. Kamada, T. Yanagida, J. Pejchal, M. Nikl, T. Endo, K. Tsutumi, Y. Fujimoto, A. Fukabori, and A. Yoshikawa, Scintillator-oriented combinatorial search in Ce-doped $(Y, Gd)_3(Ga, Al)_5O_{12}$ multicomponent garnet compounds, J. Phys. D: Appl. Phys. **44**, 505104 (2011).

[31] K. Kamada, P. Prusa, M. Nikl, K. Blazek, T. Endo, K. Tsutsumi, S. Kurosawa, Y. Yokota, and A. Yoshikawa, Czochralski growth and scintillation properties of Ce : $(Gd, Y, Lu,)_3(Al, Ga)_4O_{12}$ single crystals, IEEE Trans. Nucl. Sci. **61**, 293 (2014).

[32] P. Prusa, K. Kamada, M. Nikl, A. Yoshikawa, and J. A. Mares, Light yield of $(Lu, Y, Gd)_3Al_2Ga_3O_{12}$: Ce garnets, Radiat. Meas. **56**, 62 (2013).

[33] W. Chewpraditkul, P. Brůža, D. Pánek, N. Pattanaboonmee, K. Wantong, W. Chewpraditkul, V. Babin, K. Bartosiewicz, K. Kamada, A. Yoshikawa, and M. Nikl, Optical and scintillation properties of Ce^{3+}-doped $YGd_2Al_{5-x}Ga_xO_{12}$ $(x = 2, 3, 4)$ single crystal scintillators, J. Lumin. **169**, 43 (2016).

[34] R. R. Monchamp, The distribution coefficient on neodymium and lutetium in Czochralski grown $Y_3Al_5O_{12}$, J. Cryst. Growth **11**, 310 (1971).

[35] H. Ogino, A. Yoshikawa, M. Nikl, K. Kamada, and T. Fukuda, Scintillation characteristics of Pr-doped $Lu_3Al_5O_{12}$ single crystals, J. Cryst. Growth **292**, 239 (2006).

[36] H. Sato, K. Shimamura, V. Sudesh, M. Ito, H. Machida, and T. Fukuda, Growth and characterization of Tm, Ho-codoped $Lu_3Al_5O_{12}$ single crystals by the Czochralski technique, J. Cryst. Growth **234**, 463 (2002).

[37] Y. Kuwano, Effective distribution coefficient of neodynium in Nd : $Gd_3Ga_5O_{12}$ crystals grown by the Czochralski method, J. Cryst. Growth **57**, 353 (1982).

[38] K. Kamada, T. Yanagida, T. Endo, K. Tsutumi, Y. Usuki, M. Nikl, Y. Fujimoto, A. Fukabori, and A. Yoshikawa, 2 inch diameter single crystal growth and scintillation properties of Ce : $Gd_3Al_2Ga_3O_{12}$, J. Cryst. Growth **352**, 88 (2012).

[39] Z. Jia, X. Tao, H. Yu, C. Dong, J. Zhang, H. Zhang, Z. Wang, and M. Jiang, Growth and properties of Nd : $(Lu_xGd_{1-x})_3Ga_5O_{12}$ laser crystal by Czochralski method, Opt. Mater. **31**, 346 (2008).

[40] Z. Chen, L. Yang, Y. Hang, and X. Wang, Preparation and characterization of highly transparent Ce^{3+} doped terbium gallium garnet single crystal, Opt. Mater. **47**, 39 (2015).

[41] Y. Kuwano, S. Saito, and U. Hase, Crystal growth and optical properties of Nd: GGAG, J. Cryst. Growth **92**, 17 (1988).

[42] Q. Sai, D. Zhou, C. Xia, X. Xu, J. Di, and L. Wang, Spectroscopic properties of Nd^{3+} : $Lu_3ScAl_4O_{12}$ single crystal, Laser Phys. **23**, 115801 (2013).

[43] I. Baumann, P. Rudolph, D. Krabe, and R. Schalge, Orthoscopic investigation of the axial optical and compositional homogeneity of Czochralski grown $LiNbO_3$ crystals, J. Cryst. Growth **128**, 903 (1993).

[44] M. Kürten and J. Schilz, Czochralski growth of $SitGe_{1-x}$ single crystals, J. Cryst. Growth **139**, 1 (1994).

[45] P. S. Dutta and A. G. Ostrogorsky, Suppression of cracks in $In_xGa_{1-x}Sb$ crystals through forced convection in the melt, J. Cryst. Growth **194**, 1 (1998).

[46] I. Yonenaga, Czochralski growth of GeSi bulk alloy crystals, J. Cryst. Growth **198–199**, 404 (1999).

[47] B. Bauer and P. Gille, Crystal growth of Al-rich complex metallic phases in the system Al-Cr-Fe using the Czochralski method, Z. Anorg. Und Allg. Chem. **637**, 2052 (2011).

[48] K. Bader and P. Gille, Single crystal growth of $FeGa_3$ and $FeGa_{3-x}Ge_x$ from high-temperature solution using the Czochralski method, Cryst. Res. Technol. **55**, 1900067 (2020).

[49] C. Guguschev, D. Klimm, M. Brützam, T. M. Gesing, M. Gogolin, H. Paik, T. Markurt, D. J. Kok, A. Kwasniewski, U. Jendritzki, and D. G. Schlom, Czochralski growth and characterization of perovskite-type (La, Nd)(Lu, Sc)O_3 single crystals with a pseudocubic lattice parameter of about 4.09 Å, J. Cryst. Growth **536**, 125526 (2020).

[50] R. D. Shannon, Revised effective ionic radii and systematic studies of interatomic distances in halides and chalcogenides, Acta Crystallogr., Sect. A **32**, 751 (1976).

[51] J. G. Li and Y. Sakka, Recent progress in advanced optical materials based on gadolinium aluminate garnet ($Gd_3Al_5O_{12}$), Sci. Technol. Adv. Mater. **16**, 014902 (2015).

[52] See Supplemental Material at http://link.aps.org/supplemental/10.1103/PhysRevMaterials.5.083401 for single-crystal XRD refinement parameters.

[53] Rigaku, *CrystalClear* (Rigaku Corporation, Tokyo, 2005).

[54] G. M. Sheldrick, A short history of SHELX, Acta Crystallogr., Sect. A: Found. Crystallogr. **64**, 112 (2008).

[55] L. J. Farrugia, WINGX and ORTEP for Windows: An update, J. Appl. Crystallogr. **45**, 849 (2012).

[56] C. Chen, R. Yang, N. Sun, S. Wang, L. Fu, Y. Wang, S. Tian, Z. Huang, T. Sun, H. Liu, Y. Shi, X. Li, and H. Shao, Influence of melt convection on distribution of indium inclusions in liquid-encapsulated Czochralski-grown indium phosphide crystals, J. Mater. Sci. **31**, 20160 (2020).

[57] A. Yoshikawa, Y. Kagamitani, D. A. Pawlak, H. Sato, H. Machida, and T. Fukuda, Czochralski growth of $Tb_3Sc_2Al_3O_{12}$ single crystal for Faraday rotator, Mater. Res. Bull. **37**, 1 (2002).

[58] L. C. Lim, L. K. Tan, and H. C. Zeng, Bubble formation in Czochralski-grown lead molybdate crystals, J. Cryst. Growth **167**, 686 (1996).

[59] V. M. Orera and J. Llorca, Directionally solidified eutectic oxide ceramics, in *Encyclopedia of Materials: Science and Technology* (Elsevier, Amsterdam, 2005), pp. 1–9.

[60] P. Wu and A. D. Pelton, Coupled thermodynamic-phase diagram assessment of the rare earth oxide-aluminium oxide binary systems, J. Alloys Compd. **179**, 259 (1992).

[61] O. Fabrichnaya, H. J. Seifert, T. Ludwig, F. Aldinger, and A. Navrotsky, The assessment of thermodynamic parameters in the Al_2O_3-Y_2O_3 system and phase relations in the Y-Al-O system, Scand. J. Metall. **30**, 175 (2001).

[62] B. R. Pamplin, *Crystal Growth*, 2nd ed. (Pergamon Press, Elmsford, NY, 1980).

[63] C. D. Brandle, D. C. Miller, and J. W. Nielsen, The elimination of defects in Czochralski grown rare-earth gallium garnets, J. Cryst. Growth **12**, 195 (1972).